nature physics

Article

https://doi.org/10.1038/s41567-026-03171-0

High-order virtual gain for optical loss compensation in plasmonic metamaterials

Received: 25 May 2025

Accepted: 7 January 2026

Fuxin Guan[1,2,7] ✉, **Zemeng Lin**[2,7], **Sixin Chen**[2,7], **Xinhua Wen**[2], **Tao Li**[1] & **Shuang Zhang**[2,3,4,5,6] ✉

Metamaterials offer unprecedented control over wave propagation, but suffer from optical losses due to wave dissipation, particularly in optical imaging and sensing systems. Recent advances leveraging complex-frequency wave excitations with temporal attenuation offer promising solutions for optical loss compensation. However, this approach faces limitations in extreme loss scenarios. The complex-frequency wave requires sufficient temporal attenuation to offset material loss, inevitably triggering rapid signal decay to zero before reaching a quasi-static state. Here we engineer excitations with high-order temporal attenuation to slow down the decay rate. This allows the signal to persist for long enough to reach a quasi-static state and preserve the loss compensation efficiency. We experimentally demonstrate 20-fold noise suppression in plasmonic resonance systems compared with conventional complex-frequency excitations. This approach offers broad applicability across diverse fields, including imaging, biosensing and integrated photonic signal processing.

Optical losses pose serious constraints on various applications of plasmonics and metamaterials, including superlens imaging[1–6], optical sensing[7–11] and polaritonic information processing[12–16]. Although low-temperature experiments have been proposed as a solution to the material loss, experimental realization is fairly challenging despite some progress being made[17]. There have been some endeavours to compensate for the optical loss of plasmonics and metamaterials using gain material[18–20]. However, the required gain is unrealistic for many plasmonic systems, and gain also introduces instability and noise to the systems.

Complex-frequency waves (CFWs) have emerged as critical tools for loss compensation in superlens systems, enabling super-resolution imaging capabilities beyond conventional diffraction limits[5,21–24]. Beyond imaging applications, these engineered waveforms are further driving the discoveries of novel phenomena in wave physics[25–36]. However, excitation and measurement involving CFWs with temporally exponential attenuation present challenges in optical experiments. A practical solution has been recently proposed, involving the linear combination of the measurement results at multiple monochromatics in an appropriate manner[6]. This approach has facilitated the experimental observations of deep-subwavelength superlens imaging, ultrasensitive molecular sensing[37] and near-loss-free polaritonic propagation[38]. However, the temporally abrupt truncation at the onset of CFWs and the finite response time inherent to realistic systems necessitate a lengthy period to enter a quasi-static state, thereby minimizing unwanted noise signals. Systems with extreme losses require a substantial virtual gain, achieved through the implementation of a large imaginary frequency. This requirement induces the rapid attenuation of CFW before it stabilizes into a measurable quasi-static state, undermining the efficacy of CFW-based loss compensation. Furthermore, the finite available frequency range in measurements seriously impact the synthesis of complex-frequency results.

---

[1]National Laboratory of Solid State Microstructures, College of Engineering and Applied Sciences, Collaborative Innovation Center of Advanced Microstructures, Nanjing University, Nanjing, China. [2]New Cornerstone Science Laboratory, Department of Physics, University of Hong Kong, Hong Kong, China. [3]State Key Laboratory of Optical Quantum Materials, University of Hong Kong, Hong Kong, China. [4]Department of Electrical & Electronic Engineering, University of Hong Kong, Hong Kong, China. [5]Materials Innovation Institute for Life Sciences and Energy (MILES), HKU-SIRI, Shenzhen, China. [6]Quantum Science Center of Guangdong-Hong Kong-Macao Great Bay Area, Shenzhen, China. [7]These authors contributed equally: Fuxin Guan, Zemeng Lin, Sixin Chen. ✉e-mail: guanfuxin@nju.edu.cn; shuzhang@hku.hk

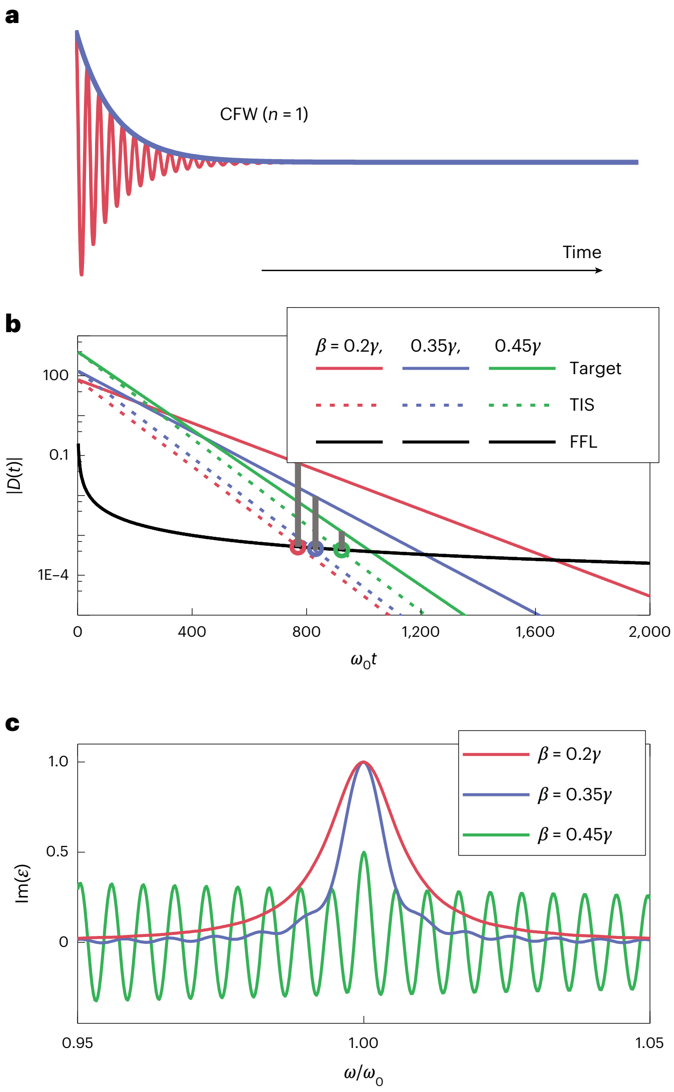

Fig. 1 | Illustration of loss compensation with CFW of different virtual gains. **a**, Temporal profile of a truncated CFW. **b**, Temporal evolutions of displacement fields of the target (coloured solid lines), TIS (coloured dashed lines) and FFL (black line) under synthesized complex-frequency excitation. The red, blue and green lines correspond to different virtual gains of $\beta = 0.2\gamma$, 0.35γ and 0.45γ, respectively. The crossing points between TIS (dashed lines) and FFL (black line) are marked by circles of different colours. The parameters of the Lorentz model are $\omega_{\mathrm{p}} = \omega_0 = 2$ and $\gamma = 0.05$. The values of the three TURs are represented by the lengths of grey vertical lines at the corresponding crossing points between the coloured dashed lines and the black solid line. **c**, Imaginary parts of the compensated permittivity $[\mathrm{Im}(\varepsilon)]$ with the three different β values at the crossing points in **b**. The integral range is $(0.5\omega_0 - 1.5\omega_0)$.

In this work, we address these limitations by engineering high-order virtual gain (HVG) excitations via the multimonochromatic synthesis approach, which corresponds to a high-power Lorentzian spectral profile in the frequency domain. The temporal pulse shape of HVG waves was theoretically proposed by Roger et al. as a solution to loss issues in metamaterials[39]. It is worth noting that high-power virtual loss has recently been harnessed for the excitation of absorbing an exceptional point[40–42]. Temporally, the synthetic HVG waveform manifests as an exponential attenuation function modulated by a temporal power-law component, dramatically mitigating the temporal attenuation. Compared with CFWs with equivalent virtual gains, HVG excitations demonstrate enhanced robustness against the limitation imposed by rapid temporal attenuation. To demonstrate this concept, we implement synthesized HVG excitations in probing plasmon-induced transparency (PIT) within optical metamaterials. Our results reveal that HVG excitation achieves 20-fold greater noise suppression compared with conventional CFWs.

Theory

We begin with a brief description of compensating loss in permittivity using synthetic complex-frequency excitation[6]. The excitation wave is a truncated CFW, $E(t) = \mathrm{e}^{-\mathrm{i}\tilde{\omega}t}\theta(t) = \int 1/[2\pi\mathrm{i}(\tilde{\omega} - \omega')]\mathrm{e}^{-\mathrm{i}\omega' t}\mathrm{d}\omega'$, where $\tilde{\omega} = \omega - \mathrm{i}\beta$, and $\beta > 0$ corresponds to the temporal attenuation factor. The corresponding field profile is shown in Fig. 1a, which takes an attenuating waveform. We consider a permittivity described by the Lorentzian form $\varepsilon_{\mathrm{L}}(\omega) = 1 - \omega_{\mathrm{p}}^2/(\omega^2 + \mathrm{i}\omega\gamma - \omega_0^2 - \gamma^2/4)$, where γ represents the damping term and ω_{p} and $\sqrt{\omega_0^2 + \gamma^2/4}$ are the plasma frequency and resonance frequency, respectively. Using the synthetic complex-frequency approach for loss compensation, the synthesized displacement field under complex-frequency excitation can be expressed as a linear combination of multifrequency response: $D(\tilde{\omega}, t) = \int_{\omega_0-\omega_\Delta}^{\omega_0+\omega_\Delta}\varepsilon_{\mathrm{L}}(\omega')\mathrm{e}^{-\mathrm{i}\omega' t}/[2\pi\mathrm{i}(\tilde{\omega} - \omega')]\mathrm{d}\omega'$, where $2\omega_\Delta$ represents the integral range, determined by the experimentally accessible frequency range for measurements. We then divide it into two parts: $D(\tilde{\omega}, t) = \int_{-\infty}^{\infty}\varepsilon_{\mathrm{L}}(\omega')\,\mathrm{e}^{-\mathrm{i}\omega' t}/\,[2\pi\mathrm{i}\,(\tilde{\omega} - \omega')]\,\mathrm{d}\omega' + D_{\mathrm{FFL}}(t)$, where $D_{\mathrm{FFL}}(t) = -(\int_{-\infty}^{\omega_0-\omega_\Delta} + \int_{\omega_0+\omega_\Delta}^{\infty})\varepsilon_{\mathrm{L}}(\omega')e^{-\mathrm{i}\omega' t}/[2\pi\mathrm{i}(\tilde{\omega} - \omega')]d\omega'$ represents the unwanted signal due to the finite-frequency limit (FFL), and can be approximated as $|D_{\mathrm{FFL}}(t)| \approx |\cos(\omega_\Delta t)|(\pi t\omega_\Delta)^{-1}$. On the basis of the residue theorem, the displacement field can be further expressed as $D(\tilde{\omega}, t) = \varepsilon_{\mathrm{L}}(\tilde{\omega})\,e^{-\mathrm{i}\tilde{\omega}t} + D_{\mathrm{TIS}}(\tilde{\omega}, t) + D_{\mathrm{FFL}}(t)$, where $D_{\mathrm{TIS}}(\tilde{\omega}, t) = \omega_{\mathrm{p}}^2 e^{-\mathrm{i}\tilde{\omega}_0 t}/\,[2\omega_0(\tilde{\omega} - \tilde{\omega}_0)]$ represents the unwanted signal caused by the synergistic result of abrupt temporal truncation and the intrinsic resonance of permittivity (TIS, truncation-induced signal). The combined term $(|D_{\mathrm{TIS}}(\tilde{\omega}, t)| + |D_{\mathrm{FFL}}(t)|)$ represents the overall unwanted signal with the multifrequency approach. In practice, it is important to minimize the impact of this term by optimizing the evolution period for taking the measurements.

The temporal evolutions of the above three terms are given by $|\varepsilon_{\mathrm{L}}(\tilde{\omega})\mathrm{e}^{-\mathrm{i}\tilde{\omega}t}| \propto \mathrm{e}^{-\ t}$ (the target), $|D_{\mathrm{TIS}}(\tilde{\omega}, t)| \propto \mathrm{e}^{-\gamma t/2}$ and $|D_{\mathrm{FFL}}(t)| \propto (\omega_\Delta t)^{-1}$. To illustrate the optimization of the evolution period, Fig. 1b shows the temporal evolution of the three terms in the logarithmic scale for a given set of parameters. To reach the quasi-steady state, it is required that $\beta < \gamma/2$ such that D_{TIS} attenuates faster than the target signal, and their ratio is represented by the difference between the solid and dashed lines of the same colour (Fig. 1b), which increases linearly with time. On the other hand, the finite-frequency effect, represented by the black solid line, remains the same for different virtual gains, and decays at a slower rate than TIS and surpasses it after a certain period. Thus, the optimal evolution time is the moment when $|D_{\mathrm{TIS}}(\tilde{\omega}, t)| = |D_{\mathrm{FFL}}(t)|$, corresponding to the crossing points between the dashed lines and the black line in Fig. 1b, which critically depends on the permittivity damping (the $\gamma/2$ term) and the available frequency range $2\omega_\Delta$. When the virtual gain is increased (blue and green lines), the ratio between the target signal and D_{TIS} at the optimal evolution time becomes lower, leading to a reduction of target-to-unwanted signal ratio (TUR), defined as the ratio between the target signal to the overall unwanted signal (represented by the length of the vertical grey lines in Fig. 1b). When β approaches $\gamma/2$ (for example, $\beta = 0.45\gamma$ in Fig. 1b), the TUR is close to unity, making loss compensation almost impossible to reach.

The imaginary parts of the compensated permittivities $\mathrm{Im}(\varepsilon)$ for the three different virtual gains at their respective crossing points are shown in Fig. 1c. $\mathrm{Im}(\varepsilon)$ with a higher imaginary frequency β (virtual gain) exhibits stronger oscillatory features due to the significant level of the unwanted signals. Thus, there exists a trade-off between the level of virtual gain and the TUR. More details are provided in Supplementary Section 1.

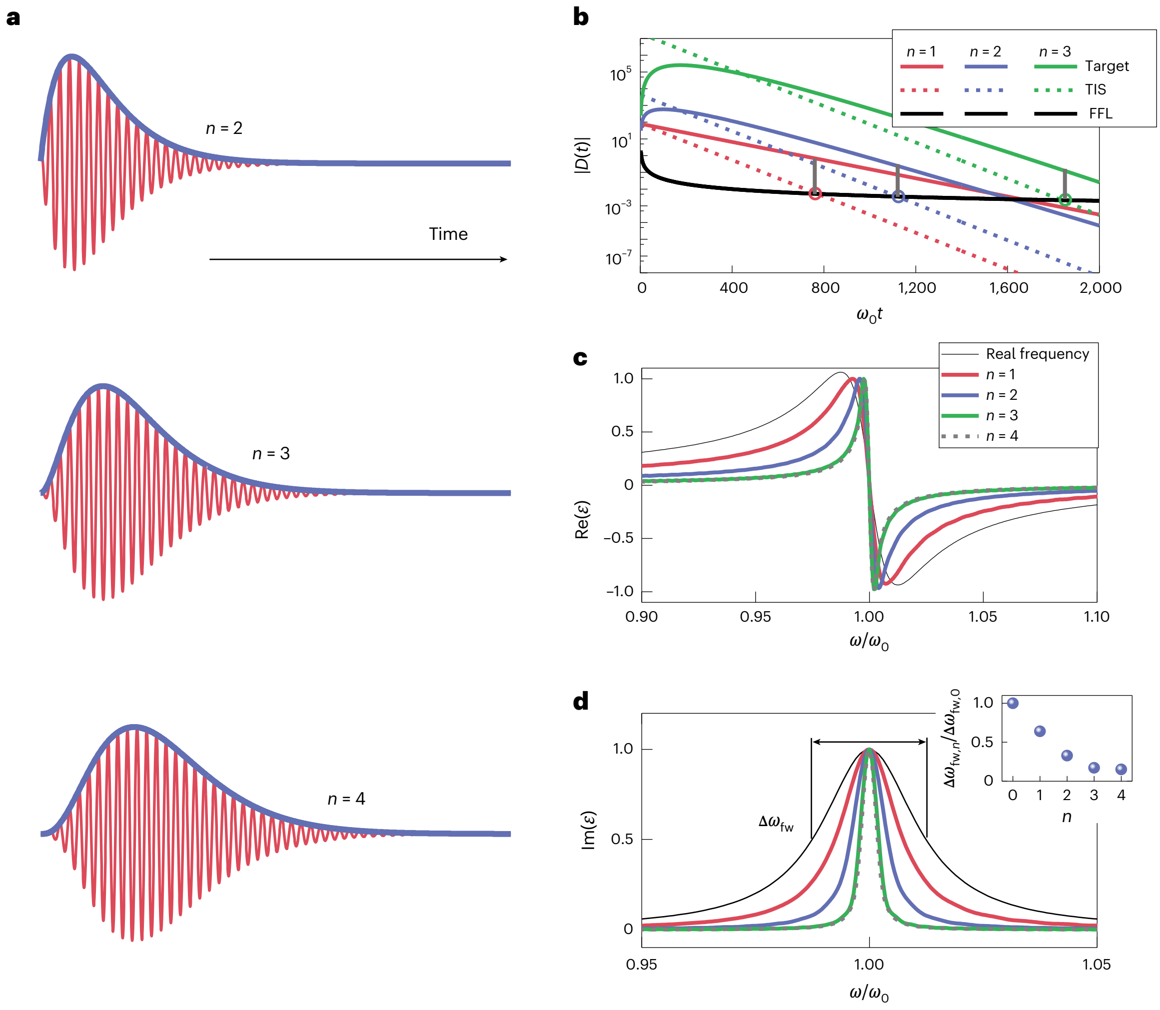

Fig. 2 | Synthetic excitations of HVGs for loss compensation. **a**, Temporal profiles of HVG waves. **b**, Temporal evolutions of the target (coloured solid lines), TIS (coloured dashed lines) and FFL (black line) under excitation of HVGs of three different orders: $n=1$, $\beta = 0.2\gamma$ (i); $n=2$, $\beta = 0.4\gamma$ (ii); $n=3$, $\beta = 0.492\gamma$ (iii). Here the FFL terms in three cases are normalized to the same curve for better comparison. **c**,**d**, Real (**c**) and imaginary (**d**) parts of the Lorentz permittivity with the synthesized excitations of HVGs. The virtual gains of different orders, ranging from $n=1$ to $n=4$, are given by $\beta_1 = 0.2\gamma$, $\beta_2 = 0.4\gamma$, $\beta_3 = 0.492\gamma$ and $\beta_4 = 0.499\gamma$, respectively. Each result is selected at the snapshot of the crossing point shown in **b**. The inset shows the dependence of the full-width at half-maximum over the orders of different virtual gains.

Next, we show how this trade-off is alleviated by using excitations with HVG. The nth-power synthetic wave takes the form $E_n(t) = t^{n-1}e^{-\mathrm{i}\widetilde{\omega}t}\theta(t)$, which can be decomposed into a Fourier form as $E_n(t) = (n-1)!\int e^{-\mathrm{i}\omega' t}/[2\pi(\mathrm{i}\widetilde{\omega} - \mathrm{i}\omega')^n]\mathrm{d}\omega'$, where $\widetilde{\omega} = \omega - \mathrm{i}\beta$. Note that for $n=1$, $E_1(t) = e^{-\mathrm{i}\widetilde{\omega}t}\theta(t)$ recovers the truncated CFW. The corresponding waveforms for $n=2$, 3 and 4 are presented in Fig. 2a. The synthesized response of the nth-order displacement field can be derived as $D_n(\widetilde{\omega}, t) = (n-1)!\int_{-\infty}^{\infty}\varepsilon_{\mathrm{L}}(\omega')\mathrm{e}^{-\mathrm{i}\omega' t}/[2\pi(\mathrm{i}\widetilde{\omega} - \mathrm{i}\omega')^n]\mathrm{d}\omega' + D_{n,\mathrm{FFL}}(t)$, where $|D_{n,FFL}(t)| = |(n-1)!(\int_{-\infty}^{\omega_0-\omega_\Delta} + \int_{\omega_0+\omega_\Delta}^{\infty})\varepsilon_{\mathrm{L}}(\omega')\mathrm{e}^{-\mathrm{i}\omega' t}/[2\pi(\mathrm{i}\widetilde{\omega} - \mathrm{i}\omega')^n]\mathrm{d}\omega'| \approx \begin{cases} (n-1)!|\cos(\omega_\Delta t)|(\pi t\omega_\Delta^n)^{-1} & n \in \text{odd} \\ (n-1)!|\sin(\omega_\Delta t)|(\pi t\omega_\Delta^n)^{-1} & n \in \text{even} \end{cases}$ comes from the FFL.

Using the high-order residue theorem, we have $D_n(\widetilde{\omega}, t) \approx t^{n-1}\varepsilon_{\mathrm{L}}(\widetilde{\omega})e^{-\mathrm{i}\widetilde{\omega}t} + D_{n,\mathrm{TIS}}(\widetilde{\omega}, t) + D_{n,\mathrm{FFL}}(t)$, where $D_{n,\mathrm{TIS}}(\widetilde{\omega}, t) = \mathrm{i}(n-1)!\omega_{\mathrm{p}}^2 e^{-\mathrm{i}\widetilde{\omega}_0 t}/[2\omega_0(\mathrm{i}\widetilde{\omega} - \mathrm{i}\widetilde{\omega}_0)^n]$ comes from the temporal TIS. The temporal evolutions of the three terms are given by $|t^{n-1}\varepsilon_{\mathrm{L}}(\widetilde{\omega})\mathrm{e}^{-\mathrm{i}\widetilde{\omega}t}| \propto \mathrm{e}^{-\beta t}t^{n-1}$ (target signal), $|D_{n,\mathrm{TIS}}| \propto \mathrm{e}^{-\gamma t/2}$ and $|D_{n,\mathrm{FFL}}| \propto (\omega_\Delta^n t)^{-1}$. The evolutions of the target and unwanted signals for HVGs of different orders are given in Fig. 2b: (i): $n=1$, $\beta = 0.2\gamma$ (red); (ii): $n=2$, $\beta = 0.4\gamma$ (blue); (iii): $n=3$, $\beta = 0.492\gamma$ (green). Here we choose different virtual gains for different orders to ensure that they have the same TUR of around 1% at their respective optimized evolution moments, where the nth displacement field can be approximated as $D_n(\tilde{\omega}, t) \approx t^{n-1}\varepsilon_{\mathrm{L}}(\tilde{\omega})e^{-\mathrm{i}\tilde{\omega}t}$ (Supplementary Sections 2 and 3). The multiplication of t^{n-1} dramatically slows down the attenuation of the excitation, making the displacement field of high orders more robust against unwanted signals arising from temporal truncation and finite-frequency range compared with complex-frequency excitation. This implies that HVG wave excitations have a more sufficient duration to reach quasi-static states compared with complex-frequency excitations. The corresponding real and imaginary parts of the compensated permittivities for $n=1$–4, together with that without loss compensation, are shown in Fig. 2c,d, respectively. The corresponding full-width at half-maximum of the imaginary permittivity $\Delta\omega_{\mathrm{fw}}$ for $n=0$–4 ($n=0$ represents the case without loss compensation) are shown in Fig. 2d (inset). It shows that by maintaining the same TUR level, the HVG excitations can lead to more effective loss compensation. For the particular set of parameters, the loss compensation starts to saturate at around $n = 3$. More detailed information for the temporal evolution of permittivity with virtual gains of different orders are presented in Supplementary Figs. 1 and 2.

It is important to note that although the above analysis is applied to permittivity, any linear responses of the system under excitation of the nth-order HVG can be synthesized via the multifrequency approach, given by

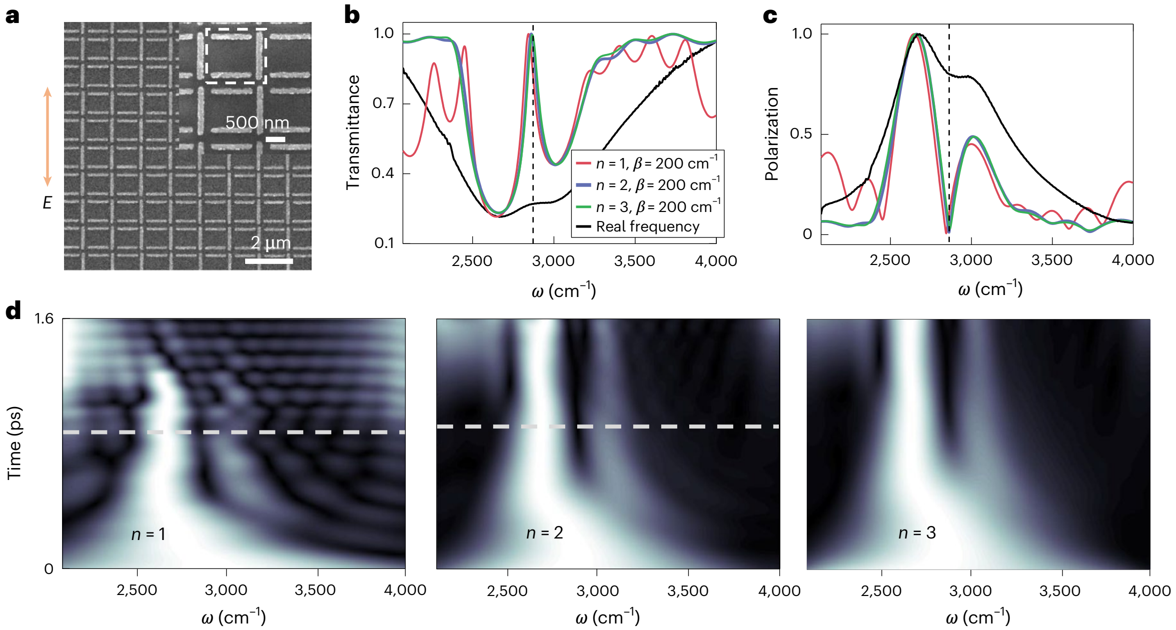

Fig. 3 | Experimental demonstration of recovering plasmonic resonances with HVG excitations. a, Scanning electron microscopy image of the fabricated PIT metamaterial. The structure inside the white dashed box shows the unit cell of the metamaterials, consisting of two parallel metal bars and a vertical metal bar. **b**,**c**, Transmittances ($\tilde{T}$ and $\tilde{T}_n$) (**b**) and polarizations ($\tilde{p}$ and $\tilde{p}_n$) (**c**) under excitations of real frequency and HVGs. The same virtual gain of $\beta = 200\ \mathrm{cm}^{-1}$ is used for all cases. The vertical dashed line indicates the simulated peak position. **d**, Temporal evolutions of polarizations $\tilde{p}_n(\tilde{\omega}, t)$ for $n = 1$–3. The spectra shown in **c** are selected at the moments indicated by the dashed lines in **d**.

$$F_n(\tilde{\omega}, t) \approx (n-1)! \sum_k \frac{F(\omega'_k)\mathrm{e}^{-\mathrm{i}\omega'_k t}\Delta\omega'_k}{2\pi(\mathrm{i}\tilde{\omega} - \mathrm{i}\omega'_k)^n}, \qquad (1)$$

where $\Delta\omega'_k$ is the frequency interval.

Loss compensation for PIT

We utilize a PIT system to further investigate the effectiveness of loss compensation using HVG. Optical sensors based on plasmonic/phononic nanostructures have been extensively investigated[11,12]. However, optical losses in the nanostructures dramatically reduce their sensitivity. Specifically, for a PIT system[43,44], plasmonic losses reduce the quality factor of the subradiant mode, leading to dramatically degraded transparency peak, which is typically used for the investigation of spectroscopy. To address this issue, we use the synthetic HVG excitation to recover the transparency peak in the measurements. The PIT metamaterial is designed following ref. 44, where each dolmen-shaped unit cell consists of coupled bright and dark elements, supporting a radiative mode and a subradiant mode, respectively (Fig. 3a). The subradiant mode is supported by two parallel metal bars (enclosed in the dashed box), whereas the radiative mode is supported by the vertical metal bar. When vertically polarized light shines on the metamaterial, it excites the radiative mode, which then couples to the subradiant mode, forming a PIT system. The nanofabrication and measurement techniques are provided in the Methods.

The measured transmission (T_{M}) spectrum of the PIT sample is presented in Fig. 3b (black curve). Due to the existence of significant plasmonic loss, the transparency peak at around 2,850 cm−1 is barely visible. To compensate for the plasmonic loss using the synthesized HVG excitation, an intermediate polarization parameter $\tilde{p}(\omega) = \mathrm{i}(\frac{1}{\tilde{t}_{\mathrm{M}}(\omega)} - \frac{1}{t_0})$ is used, similar to the approach used in ref. 37, where $\tilde{t}_{\mathrm{M}}(\omega) = \mathrm{e}^{\mathrm{i}\varphi_{\mathrm{M}}}\sqrt{T_{\mathrm{M}}}$ corresponds to the transmission coefficient, and the phase term φ_M is obtained using the Kramers–Kronig relations[45]. The parameter $t_0 \approx 2/(1+n_{\mathrm{s}})$ denotes the transmission coefficient of the pure substrate[46], where $n_{\mathrm{s}} \approx 1.35$ corresponds to the refractive index of substrate made of fused silica. The magnitude of the calculated polarization term $\tilde{p}(\omega)$ is shown in Fig. 3c (black line).

We substitute $\tilde{p}(\omega)$ into equation (1) to obtain $\tilde{p}_n(\tilde{\omega}, t)$ of different orders, and the corresponding temporal evolution of their magnitudes is shown in Fig. 3d for $n = 1$–3, with the same virtual gain of 200 cm−1. The polarization $\tilde{p}_1(\tilde{\omega}, t)$ exhibits fairly significant unwanted oscillatory features over time and frequency, whereas the oscillatory features are very small for $\tilde{p}_2(\tilde{\omega}, t)$ and $\tilde{p}_3(\tilde{\omega}, t)$. For these cases, we select the temporal snapshots in Fig. 3d (white dashed lines) to obtain the compensated polarizations, which are plotted as the red, blue and green lines in Fig. 3c. The corresponding transmittances $|\tilde{T}_n(\tilde{\omega}, t)|$ are plotted in Fig. 3b as the red, blue and green lines. Although the excitation of $n = 1$ can recover the PIT peak in the transmission spectrum, the oscillatory features dramatically reduce the TUR. On the other hand, the HVG excitations of $n = 2$ and 3 greatly enhance the TUR of the transmittance, exhibiting loss compensated spectra with good quality.

We also fabricated another sample with a weaker coupling (Extended Data Fig. 1) for comparison. In Extended Data Fig. 1a,b, the double-peak features in the spectra (black lines) are much more blurred than the measured spectra in Fig. 3, indicating that recovering the loss with the HVG approach is more challenging for this sample. Therefore, we optimize the β value separately for each order n to achieve the best performance, the optimized β values are shown in the inset. The polarization evolutions are shown in Extended Data Fig. 1c, where unwanted noise appears earlier and more prominently than that in Fig. 3. Using an adaptive temporal snapshot at the dashed-line position for each case, we plot the results for different orders in Extended Data Fig. 1a,b. The results for $n = 2$ and $n = 3$ clearly exhibit double-peak behaviour with fairly low unwanted noise, whereas the $n = 1$ result fails to resolve the dip.

Additionally, we also use this approach to examine the imaging resolution of the microwave hyperbolic lens. The results are shown in Supplementary Section 4. The third-order virtual gain wave excitation clearly reconstructs the ground truth more accurately than the first-order wave excitation, whereas the real frequency wave does not. These findings further demonstrate the advantages of the HVG approach.

Summary

We have proposed synthetic waves of HVG to compensate for the intrinsic losses of plasmonic metamaterials, achieving 20-fold noise suppression in transmission spectra, which surpasses the performance attainable with conventional complex-frequency excitation. Our approach effectively resolves the spectral oscillations induced by temporal truncation and finite-frequency limitations in synthesized complex-frequency excitations, demonstrating its potential for high-precision spectroscopy and molecule sensing. This approach is broadly applicable to loss mitigation in plasmonic, phononic and excitonic systems, enabling long-distance polaritonic propagations and facilitating advancements in on-chip photonics. Moreover, it can be extended to other wave regimes, including acoustic and hydrodynamic waves.

Online content

Any methods, additional references, Nature Portfolio reporting summaries, source data, extended data, supplementary information, acknowledgements, peer review information; details of author contributions and competing interests; and statements of data and code availability are available at https://doi.org/10.1038/s41567-026-03171-0.

References

1. Pendry, J. B. Negative refraction makes a perfect lens. *Phys. Rev. Lett.* **85**, 3966–3969 (2000).
2. Fang, N., Lee, H., Sun, C. & Zhang, X. Sub–diffraction-limited optical imaging with a silver superlens. *Science* **308**, 534–538 (2005).
3. Liu, Z., Lee, H., Xiong, Y., Sun, C. & Zhang, X. Far-field optical hyperlens magnifying sub-diffraction-limited objects. *Science* **315**, 1686 (2007).
4. Taubner, T., Korobkin, D., Urzhumov, Y., Shvets, G. & Hillenbrand, R. Near-field microscopy through a SiC superlens. *Science* **313**, 1595 (2006).
5. Kim, S., Peng, Y., Yves, S. & Alù, A. Loss compensation and super-resolution with excitations at complex frequencies. *Phys. Rev. X* **13**, 041024 (2023).
6. Guan, F. et al. Overcoming losses in superlenses with synthetic waves of complex frequency. *Science* **381**, 766–771 (2023).
7. Liu, N. et al. Plasmonic analogue of electromagnetically induced transparency at the Drude damping limit. *Nat. Mater.* **8**, 758–762 (2009).
8. Liu, N., Mesch, M., Weiss, T., Hentschel, M. & Giessen, H. Infrared perfect absorber and its application as plasmonic sensor. *Nano Lett.* **10**, 2342–2348 (2010).
9. Rodrigo, D. et al. Mid-infrared plasmonic biosensing with graphene. *Science* **349**, 165–168 (2015).
10. Sreekanth, K. V. et al. Extreme sensitivity biosensing platform based on hyperbolic metamaterials. *Nat. Mater.* **15**, 621–627 (2016).
11. Tittl, A. et al. Imaging-based molecular barcoding with pixelated dielectric metasurfaces. *Science* **360**, 1105–1109 (2018).
12. Basov, D. N., Fogler, M. M. & García De Abajo, F. J. Polaritons in van der Waals materials. *Science* **354**, aag1992 (2016).
13. Bozhevolnyi, S. I., Volkov, V. S., Devaux, E., Laluet, J. Y. & Ebbesen, T. W. Channel plasmon subwavelength waveguide components including interferometers and ring resonators. *Nature* **440**, 508–511 (2006).
14. Oulton, R. F. et al. Plasmon lasers at deep subwavelength scale. *Nature* **461**, 629–632 (2009).
15. Fei, Z. et al. Gate-tuning of graphene plasmons revealed by infrared nano-imaging. *Nature* **487**, 82–85 (2012).
16. Hu, H. et al. Gate-tunable negative refraction of mid-infrared polaritons. *Science* **379**, 558–561 (2023).
17. Ni, G. X. et al. Fundamental limits to graphene plasmonics. *Nature* **557**, 530–533 (2018).
18. Xiao, S. et al. Loss-free and active optical negative-index metamaterials. *Nature* **466**, 735–738 (2010).
19. Hamm, J. M., Wuestner, S., Tsakmakidis, K. L. & Hess, O. Theory of light amplification in active fishnet metamaterials. *Phys. Rev. Lett.* **107**, 167405 (2011).
20. Sadatgol, M., Özdemir, ŞK., Yang, L. & Güney, D. O. Plasmon injection to compensate and control losses in negative index metamaterials. *Phys. Rev. Lett.* **115**, 035502 (2015).
21. Archambault, A., Besbes, M. & Greffet, J. J. Superlens in the time domain. *Phys. Rev. Lett.* **109**, 097405 (2012).
22. Ghoshroy, A., Özdemir, ŞK. & Güney, D. Ö Loss compensation in metamaterials and plasmonics with virtual gain [invited]. *Opt. Mater. Express* **10**, 1862–1880 (2020).
23. Tetikol, H. S. & Aksun, M. I. Enhancement of resolution and propagation length by sources with temporal decay in plasmonic devices. *Plasmonics* **15**, 2137–2146 (2020).
24. An, S., Liu, T., Zhu, J. & Cheng, L. Complex-frequency calculation in acoustics with real-frequency solvers. *Phys. Rev. B* **111**, L020301 (2025).
25. Tsakmakidis, K. L., Pickering, T. W., Hamm, J. M., Page, A. F. & Hess, O. Completely stopped and dispersionless light in plasmonic waveguides. *Phys. Rev. Lett.* **112**, 167401 (2014).
26. Baranov, D. G., Krasnok, A. & Alù, A. Coherent virtual absorption based on complex zero excitation for ideal light capturing. *Optica* **4**, 1457–1461 (2017).
27. Li, H., Mekawy, A., Krasnok, A. & Alù, A. Virtual parity-time symmetry. *Phys. Rev. Lett.* **124**, 193901 (2020).
28. Trainiti, G., Radi, Y., Ruzzene, M. & Alù, A. Coherent virtual absorption of elastodynamic waves. *Sci. Adv.* **5**, eaaw3255 (2019).
29. Kim, S., Lepeshov, S., Krasnok, A. & Alù, A. Beyond bounds on light scattering with complex frequency excitations. *Phys. Rev. Lett.* **129**, 203601 (2022).
30. Gu, Z. et al. Transient non-Hermitian skin effect. *Nat. Commun.* **13**, 7668 (2022).
31. Hinney, J. et al. Efficient excitation and control of integrated photonic circuits with virtual critical coupling. *Nat. Commun.* **15**, 2741 (2024).
32. Kim, S., Krasnok, A. & Alù, A. Complex-frequency excitations in photonics and wave physics. *Science* **387**, eado4128 (2025).
33. Basov, D. N. & Fogler, M. M. 'The unreasonable effectiveness of mathematics' in evading polaritonic losses. *Nat. Mater.* **23**, 445–446 (2024).
34. Cheng, Q. & Li, T. Complex-frequency waves: beat loss and win sensitivity. *Light Sci. Appl.* **13**, 40 (2024).
35. Zouros, G. P., Loulas, I., Almpanis, E., Krasnok, A. & Tsakmakidis, K. L. Anisotropic virtual gain and large tuning of particles' scattering by complex-frequency excitations. *Commun. Phys.* **7**, 283 (2024).
36. Loulas, I., Psychogiou, E.-C., Tsakmakidis, K. L. & Stefanou, N. Analytic theory of complex-frequency-aided virtual absorption. *Opt. Express* **33**, 28333–28342 (2025).
37. Zeng, K. et al. Synthesized complex-frequency excitation for ultrasensitive molecular sensing. *eLight* **4**, 1 (2024).
38. Guan, F. et al. Compensating losses in polariton propagation with synthesized complex frequency excitation. *Nat. Mater.* **23**, 506 (2024).
39. Rogov, A. & Narimanov, E. Space–time metamaterials. *ACS Photonics* **5**, 2868–2877 (2018).
40. Farhi, A., Mekawy, A., Alù, A. & Stone, D. Excitation of absorbing exceptional points in the time domain. *Phys. Rev. A* **106**, L031503 (2022).
41. Farhi, A., Cerjan, A. & Stone, A. D. Generating and processing optical waveforms using spectral singularities. *Phys. Rev. A* **109**, 013512 (2024).
42. Farhi, A., Dai, W., Kim, S., Alù, A. & Stone, D. Efficient general waveform catching by a cavity at an absorbing exceptional point. *Phys. Rev. A* **109**, L041502 (2024).

43. Fleischhauer, M., Imamoglu, A. & Marangos, P. J. Electromagnetically induced transparency: optics in coherent media. *Rev. Mod. Phys.* **77**, 633–673 (2005).
44. Zhang, S., Genov, D. A., Wang, Y., Liu, M. & Zhang, X. Plasmon-induced transparency in metamaterials. *Phys. Rev. Lett.* **101**, 047401 (2008).
45. Gralak, B., Lequime, M., Zerrad, M. & Amra, C. Phase retrieval of reflection and transmission coefficients from Kramers–Kronig relations. *J. Opt. Soc. Am. A* **32**, 456–462 (2015).
46. Zheng, G. et al. Metasurface holograms reaching 80% efficiency. *Nat. Nanotechnol.* **10**, 308–312 (2015).

Methods

Nanofabrication of PIT metamaterials

The samples are fabricated using an electron-beam writer (TESCAN MIRA 3 with ELPHY Plus) on a silica substrate. Before pattern transfer, the substrate undergoes a thorough cleaning process. This involves consecutively cleaning with acetone, isopropanol (IPA), ethanol and deionized (DI) water, followed by drying with N_2 gas. To enhance the hydrophilicity of the substrate surface, an ozone treatment is conducted for 5 min. Next, a positive resist called PMMA 950 A3 is spin coated onto the substrate at a speed of 3,000 r.p.m. The coated substrate is then subjected to soft-baking at 160 °C for 90 s. Due to the non-conductive nature of the substrate, a thin layer of conductive material is spin coated on top of the electron-beam resist. The electron-beam exposure is performed using the electron-beam lithography, with a dose of 300 $\mu C\ cm^{-2}$ and a write field of 200 μm. Following the exposure, the conductive layer is removed by dipping the samples into DI water for a few seconds and drying with N_2 gas. The samples then undergo a development process using a developer solution made of IPA and DI water, with a weight ratio of 3:1. The development process consists of immersing the samples in the solution for 20 s at zero degrees, followed by fixing in IPA for another 20 s. The samples are then dried with N_2 gas. To deposit the desired materials—chromium and gold—onto the samples, thermal physical deposition is used. Chromium is deposited with a thickness of 5 nm, followed by the deposition of gold with a thickness of 30 nm. The lift-off process is carried out in hot acetone (60 °C) using ultrasonic agitation. After lift-off, the samples are cleaned using IPA, ethanol and DI water to ensure the removal of any residues or impurities. The process flow of fabrication is shown in Supplementary Fig. 3.

Fourier transform infrared spectroscopy measurement

The optical transmission spectra of the PIT samples are obtained using Fourier transform infrared spectroscopy. To perform these measurements, a Vertex 70 instrument equipped with Hyperion 3000 Microscopy (×15 objective) is used, which has a tunable iris size. Each sample has an array size of 200 μm, matching the iris size, to ensure an acceptable signal-to-noise ratio. The iris size of 200 μm is maintained consistently for all the measurements. To achieve the desired polarization, the incident light is polarized vertically (parallel to the bright mode atom) using a thin-film polarizer (LPMIR100, Thorlabs), which operates in the mid-infrared range with high efficiency and a large extinction ratio. Averaging signals are used to smooth the spectrum, with 254 scans performed at a resolution of 4 cm^{-1}. To normalize the spectrum, the pure fused silica substrate without patterns is used as a reference.

Data availability

The experimental data are available via Figshare at https://doi.org/10.6084/m9.figshare.30858479.

Code availability

The codes are available via Figshare at https://doi.org/10.6084/m9.figshare.30866405.

Acknowledgements

We are grateful to K. Zheng and S. Zhou for illuminating discussions. This work was supported by the New Cornerstone Science Foundation (S.Z.), National Natural Science Foundation of China (numbers 62325504 and 62288101; T.L.), the Research Grants Council of Hong Kong (AoE/P-502/20, STG3/E-704/23-N, 17309021; S.Z.) and Guangdong Provincial Quantum Science Strategic Initiative (GDZX2204004 and GDZX2304001; S.Z.).

Author contributions

S.Z. and F.G. conceived the project and supervised the overall projects. Z.L. fabricated the PIT samples and carried out the Fourier transform infrared spectroscopy experiment. F.G. and S.C. performed the numerical simulations and analytical calculations. F.G. performed the microwave experiments. F.G., Z.L., S.C., X.W., T.L. and S.Z. participated in the analysis of the results. F.G. and S.Z. wrote the manuscript with input from all authors. All authors contributed to the discussion.

Competing interests

The authors declare no competing interests.

Additional information

Extended data is available for this paper at https://doi.org/10.1038/s41567-026-03171-0.

Supplementary information The online version contains supplementary material available at https://doi.org/10.1038/s41567-026-03171-0.

Correspondence and requests for materials should be addressed to Fuxin Guan or Shuang Zhang.

Peer review information *Nature Physics* thanks Seunghwi Kim, Yu-Gui Peng and the other, anonymous, reviewer(s) for their contribution to the peer review of this work.

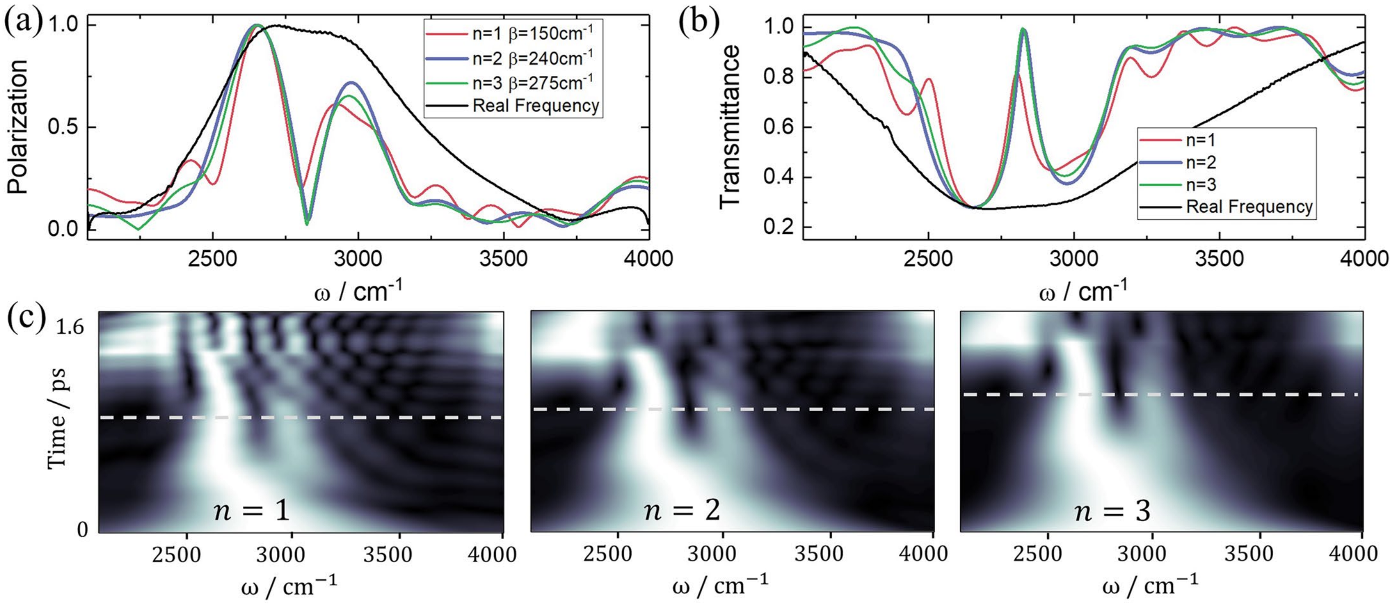

Extended Data Fig. 1 | Recovering plasmonic resonances with HVG excitations in a weaker coupling case compared with Fig. 3. (**a**) Polarizations ($\tilde{p}$ and $\tilde{p}_n$) and (**b**) transmittances ($\tilde{T}$ and $\tilde{T}_n$) under excitation of real frequency and different orders of HVG. The virtual gains with different β are displayed in the inset. (**c**) The temporal evolutions of polarizations $\tilde{p}_n(\tilde{\omega}, t)$ for $n = 1, 2$, and 3. The spectra shown in (**a**) are selected at the moments indicated by the dashed lines in (**c**).